



Conventional and neural network-based water vapor density model for GNSS troposphere tomography

Chen Liu^{1,2} · Yibin Yao^{1,3} · Chaoqian Xu¹

Received: 31 March 2021 / Accepted: 28 September 2021 / Published online: 23 October 2021
© Springer-Verlag GmbH Germany, part of Springer Nature 2021

Abstract

Global navigation satellite system (GNSS) water vapor (WV) tomography is a promising technique to reconstruct the three-dimensional (3D) WV field. However, this technique usually suffers from the ill-posed problem caused by the poor geometry of GNSS rays, resulting in underdetermined tomographic equations. Such equations often rely on iterative methods for solving, but conventional iterative approaches require accurate initial WV density. To address this demand, we proposed two models for WV density estimation. One is the conventional model (CO model) that consists of an exponential model and a linear least-squares model, which are used to describe the spatial and temporal variability of the WV density, respectively. The other is a neural network model (NN model) that uses a backpropagation neural network (BPNN) to fit the nonlinear variation of WV density in both spatial and temporal domains. WV density derived from a Hong Kong (HK) radiosonde station (RS) during 2020 was used to validate the proposed models. Validation results show that both models well describe the spatial and temporal distribution of the WV density. The NN model exhibits better prediction performance than the CO model in terms of root mean square error (RMSE) and bias. We also applied the proposed models to GNSS WV tomography to test their performance in extreme weather conditions. Test results show that the proposed model-based GNSS tomography can correct the content of WV density but cannot accurately sense its irregular distribution.

Keywords GNSS · Troposphere tomography · Water vapor density model · Radiosonde · Neural network

Introduction

The global navigation satellite system (GNSS) technique has emerged as a powerful sensor for dynamic water vapor (WV) detection (Bevis et al. 1992; Rocken et al. 1993). According to the wet ingredients within the tropospheric delay, the technique can retrieve the WV in the GNSS-ray path. Numerous studies have validated the GNSS-derived WV by comparing it with the accurate WV determined using other approaches (Chen and Liu 2016; Dai et al. 2002; Gurbuz and

Jin 2017; Troller 2004), including radiosonde, WV radiometer, and remote sensing. In addition, the widespread deployment of continuously operating reference station (CORS) systems further expands the unique superiority of the GNSS WV detection technology, for example, all-time/all-weather support and real-time continuity (Chen and Liu 2014).

Two WV products can currently be derived using the GNSS technique. One is the precipitable WV (PWV), which has been applied in many cases, e.g., weather forecasting (Zhao et al. 2021) and multi-source WV data fusion (Zhang and Yao 2021). The other is WV density obtained by the tomography algorithm, which is appropriate for assimilation into the initial field of the numerical weather prediction (NWP) system. Therefore, since it was first reported in Flores et al. (2000), GNSS WV tomography has increasingly attracted substantial interest. However, due to the less than ideal distribution of satellites and GNSS receivers, the technique still suffers an ill-posed problem within the tomographic design matrix. Various attempts have been made to overcome this problem. Dong and Jin (2018) adopted GNSS observations from multiple

✉ Yibin Yao
ybyao@whu.edu.cn

¹ School of Geodesy and Geomatics, Wuhan University, Wuhan 430079, China

² Guangxi Key Laboratory of Spatial Information and Geomatics, Guilin University of Technology, Guilin 541004, China

³ Key Laboratory of Geospace Environment and Geodesy, Ministry of Education, Wuhan University, Wuhan 430079, China

systems (GPS, BDS, GLONASS) jointly contributing to the WV tomography process; their experiment in Hong Kong (HK), China, validated its resultant three-dimensional (3D) WV information. Additionally, Yao et al. (2020a, b) developed two modified tomographic methods using an improved tomographic window and an optimized voxel strategy, respectively. The test results indicated that both modified methods achieved a superior 3D WV field than the traditional approach.

Even with the progress from the above studies, the ill-posed problem has not been completely overcome. As a result, the tomography equations still require an iterative method to solve. The main iterative algorithms commonly used in GNSS tomography, such as the multiplicative algebraic reconstruction technique (MART) (Bender et al. 2011) and Kalman filtering (KF) method (Ding et al. 2007; Nilsson and Gradinarsky 2006), all require high-quality initial values. Unfortunately, the easily accessed ERA5 and atmospheric sounding datasets do not support the real-time need for GNSS WV tomography. Also, there are no appropriate models available for WV density estimation. Therefore, even as crucial prior information, far too little attention has been paid to investigating the empirical WV density distribution of interest.

The specific objective of this study was to develop the WV density model for providing the high-quality prior WV information that used in GNSS WV tomography. With the assistance of the model, GNSS tomography can continuously perform without relying on other WV data (initial value). In this study, we established two regional WV density models. One is the conventional (CO) model, which adopted an exponential function to describe the spatial variability of WV density while imposing a linear least-squares sine and cosine model to express the temporal variability of the WV density. The other is a neural network (NN) model that used a backpropagation NN (BPNN) (Haykin 1998; Zhang et al. 2018) to fit the nonlinear variation of WV density in both temporal and spatial domains. The HK radiosonde station (RS)-derived WV density from 2015 to 2019 was used to generate the two models. Then, according to the RS record in 2020, we designed and carried out test experiments to evaluate and compare the performances of the proposed models. Also, to assess the applicability of the proposed model-based GNSS WV tomography in extreme weather, the experiments were carried out in HK when the models provided poor initial values (WV density estimation).

We first present the methodology of GNSS WV tomography and the development process for the CO and NN models, respectively. The validation of both models is described in the next section. The tomography experiment, which assisted with the proposed models, is then performed. Finally, we summarize the conclusions and outlook of this research.

GNSS troposphere WV tomography

The slant WV (SWV), which refers to the WV content in the GNSS-ray propagation path, is the fundamental data for GNSS WV tomography. After dividing the tomography area into finite voxels, the SWVs combine with their corresponding signal intercepts, forming the basic tomography equation:

$$\text{SWV}^m = \sum_{ijk} \left(A_{ijk}^m \cdot X_{ijk} \right) \quad (1)$$

where SWV^m stands for the SWV of a signal m , A_{ijk}^m refers to the intercept of the signal m in the 3D voxel (i, j, k) , and X_{ijk} is the WV density of the above voxel. Significantly, the signal line intercepts are determined by the spatial voxel strategy, which contains the horizontal and vertical grid schemes of the study area.

The constraints, which originate from the empirical WV distribution, are another essential component of the tomography equation. The three commonly imposed constraints are horizontal, vertical, and boundary conditions (Flores et al. 2000). Given the previously proposed optimized voxel (Yao et al. 2020a), the improved tomographic algorithm no longer relies heavily on the former two constraints. Thus, we now only introduce the following expression to assemble the vertical constraints (Elosegui et al. 1998):

$$\frac{V_n}{V_{n-1}} = e^{(h_{n-1}-h_n)/H} \quad (2)$$

where V_n and V_{n-1} are the WV densities of the two vertically adjacent voxels n and $n-1$, respectively; similarly, h_{n-1} and h_n are the heights of the adjacent voxels. In addition, H represents the WV-scale height. We note here that the WV scale is the critical parameter in the CO model, and its computational method is described in the below in a separate section. The appropriate number of (2) form the completed vertical constraints:

$$V \cdot X = 0 \quad (3)$$

where V is the vertical constraint matrix and X refers to the WV density of each voxel that consists of a single column vector whose rows are equal to the number of valid voxels.

Finally, Equations (1) and (3) are combined to establish the entire tomography equation:

$$\begin{aligned} A_{\text{upd}} X &= Y_{\text{upd}} \\ A_{\text{upd}} &= \begin{bmatrix} A \\ V \end{bmatrix}, Y_{\text{upd}} = \begin{bmatrix} \text{SWV} \\ 0 \end{bmatrix} \end{aligned} \quad (4)$$

where A_{upd} is the updated design matrix which consists of the GNSS ray intercept matrix A and vertical constraint matrix V , A is an $m \times n$ matrix, m is the quantity of the valid

signal while n is equal to the number of objective voxels, SWV is an $m \times 1$ column vector whose components are the SWV estimation of the m ray paths, and X is the same as in (3).

Since the significant inverse difficulties, previous research (Dong and Jin 2018) preferred the iterative method to solve (4). Hence, we selected the widespread KF algorithm for the tomography solution. The specific design and usage of KF can be found in Gradinarsky and Jarlemark (2004). Notability, the KF method requires accurate prior WV information. As a result, developing a WV density model is necessary to address the demand for GNSS tomography.

Regional WV density model

In this section, we first briefly describe the study area, list the modeling steps of the CO and NN models, and then present the modeling process of the above models.

Study area

In consideration of the comprehensive historical records of the King’s Park RS (station code: 45004) and the conveniently accessed GNSS observations of HK CORS (SatRef), we selected HK, China, as the study area. As shown in Fig. 1, there are 19 sites of SatRef and one RS in HK. The 19 evenly distributed sites, approximately 10 km of mean geographic distance between each other, can provide a massive valid signal with SWV for the tomography experiments. Meanwhile, the RS can offer sufficient high-precision 3D WV density data to establish the WV density model and as a reference for the WV tomography test.

Modeling steps

Figure 2 shows the schematic process for generating the CO and NN models. For the CO model, we first need to know the spatial and temporal distribution of WV density and then describe the above two distributions separately using the appropriate models. Combining the above models, we finally embody the entire CO model.

Regarding the NN model, the input and output datasets need to be identified first. In particular, we must clarify the variables in the input. Second, we need to define the NN structure, including the optimal number of neurons in the hidden layer. Based on the above input–output datasets and the NN structure, we finally trained and obtained the NN model.

Development of the CO model

The CO model, which consists of an exponential model and a linear least-squares model, was established in this section. Its detailed modeling steps are as follows:

Determining the WV density distribution

To model the WV density, we need to recognize the spatial and temporal variation features. Figure 3 provides the WV density variations in HK during 2015–2019. First, in the top panel, we discover that the WV density rapidly decreased with height and may have a periodicity in the timeline views. Second, the middle panel presents the exponential decrease in WV density with increasing height more distinctly than the top panel. Third, the WV densities at various layers seen in the bottom panel jointly suggest that the WV density has a similar annual periodic variation in each height layer. Therefore, integrating the contents of the figure, we may conclude the WV density varies exponentially and annually periodic in spatial and temporal domains, respectively.

Describing the spatial variability

According to Elosegui et al. (1998) and Tomasi (1981), we impose the following exponential equation to represent the spatial distribution of the WV density during a single epoch:

$$\rho_z = \rho_0 e^{-z/H} \tag{5}$$

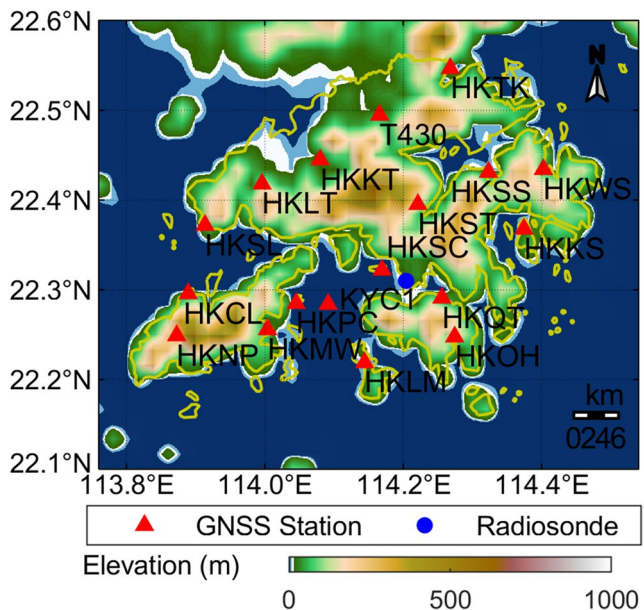
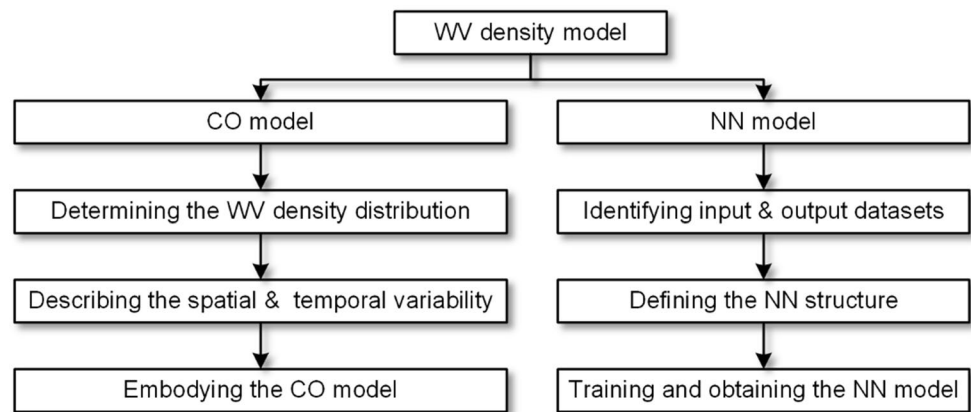


Fig. 1 Distribution of 19 GNSS stations (red triangles) and one RS (blue circle) in the selected study area

Fig. 2 Flowchart of the main procedures to establish the CO and NN models



where ρ_z and ρ_0 are the WV density at the height z and the surface WV density, respectively, and H represents the WV scale height (recall 2).

Describing the temporal variability

Based on (5), after determining the temporal variability of ρ_0 and H , we will ultimately generate the spatio-temporal WV density model. The surface WV density (ρ_0) can be retrieved from the RS record, and the WV scale height (H) can be calculated as:

$$H \approx \frac{\text{PWV}}{\rho_0} \quad (6)$$

where PWV can also be obtained directly from the RS observations. According to (6), we next need to represent the temporal variability of ρ_0 and PWV.

We executed the Lomb-Scargle (LS) method (Hocke 1998; Zhao et al. 2018) to analyze the oscillations of ρ_0 and PWV, respectively. Figure 4 shows the variations in ρ_0 (top left) and PWV (bottom left) during 2015–2019 and their corresponding power spectra (top right) and (bottom right). One distinct peak is observed at one year in both Fig. 4 (right panels), which is much higher than the 99% level, demonstrating that both ρ_0 and PWV indeed have a forceful annual variation. Based on the variabilities detected above, we introduced linear least-squares sine and cosine equations to express the oscillations:

$$\begin{aligned} x(t) &= A_0 + A_1 \sin(2\pi \cdot t) + A_2 \cos(2\pi \cdot t) \\ t &= \text{DOY}/365.25 \end{aligned} \quad (7)$$

where $x(t)$ is the ρ_0 or PWV, A_i ($i=0, 1, 2$) refers to the model coefficients, and DOY represents day-of-year (DOY).

In a word, based on the RS records during 2015–2019, we first obtained the time series model of ρ_0 and PWV. We then embodied the H model by the two models above. Integrating

the H and ρ_0 models with (5), we finally generated the entire CO model.

Development of the NN model

Multilayer NN is a powerful nonlinear fitting tool. We thereby used a BPNN to construct the NN model, whose specific modeling steps are presented as follows:

Identifying input and output datasets

According to Fig. 3, WV density varies with time and height. Therefore, the date variables (year and DOY) combined with the height variables (12 layers per epoch) were determined as the inputs. Then, we select the WV density at the height corresponding to the inputs as the outputs. Based on the identified inputs and outputs, WV density derived from HK RS record during 2015–2019 assembled the original input–output datasets.

Additionally, Fig. 3 shows that the WV density exhibits a nominal value when the height exceeds 10 km, suggesting that it is unnecessary to include more than 10 km of the WV results in the input–output datasets. We accordingly removed the above useless portion of the original input–output datasets.

Defining the NN structure

Based on the features of the input–output datasets, we adopted a BPNN to establish the NN model, which is well-performed in fitting complex nonlinear relationships (Ding 2018).

A BPNN is usually composed of the input layer, hidden layer, and output layer. With the multilayered structure, the BPNN can obtain a function that appropriately maps the given inputs to their corresponding outputs. The architecture of the BPNN used in this study is expressed in Fig. 5.

Fig. 3 Variation of WV density with time and height. The top panel uses a two-dimensional (2D) pseudo-color plan showing the above variation. The middle panel displays the specific variations in three dimensions, and the bottom panel presents the variation in specific height layers

Figure 5 shows that the input layer consists of 14 neurons, including two data parameters (year and DOY) and 12 height parameters. Accordingly, 12 neurons in the output layer match the 12 heights within the inputs. Regarding the hidden layer, a single unit can describe the nonlinear variation of WV density in both spatial and temporal domains. Next, the optimal number of neurons in hidden units requires determination. Here is a thumb rule (Masters 1994) for approximately computing the above number, i.e., $\sqrt{n \times m}$, where n and m represent the number of neurons in the input and output layer, respectively. In this case, n is 14 while m is 12, so the optimal nodes in the hidden layer may be around 13. Therefore, we tested the BPNNs with from 8 to 18 nodes in the hidden layer to obtain the best nodes setting using the tenfold cross-validation (CV) technique. This method first divides the samples, which refers to RS data from January 2015 to December 2019, randomly into an equal number of ten groups. One of the groups is then adopted as a test dataset, while the rest is used as training datasets to generate the model. This process will repeat until each individual group has been used as a test dataset. Finally, the evaluation of the model performance will be represented by the average of the ten rounds. The root mean square error (RMSE) of the BPNNs with different hidden nodes is depicted in Fig. 6. It shows that for the BPNN model, the RMSE first decreased until the number of hidden layer neurons reached 15 and then increased. This result indicates that 15 is the optimal number of neurons in hidden units. Consequently, the hidden layer with 15 neurons in a single layer is finally determined.

Among the input–output datasets acquired above, 70% were randomly divided as training, while the rest as validation. Based on the above datasets, we then trained and constructed the NN model.

Model validation experiments

RS-derived WV density during 2020 was used to validate the predicted performance of both the CO and NN models, and the comparison between them is expressed below in bias and RMSE.

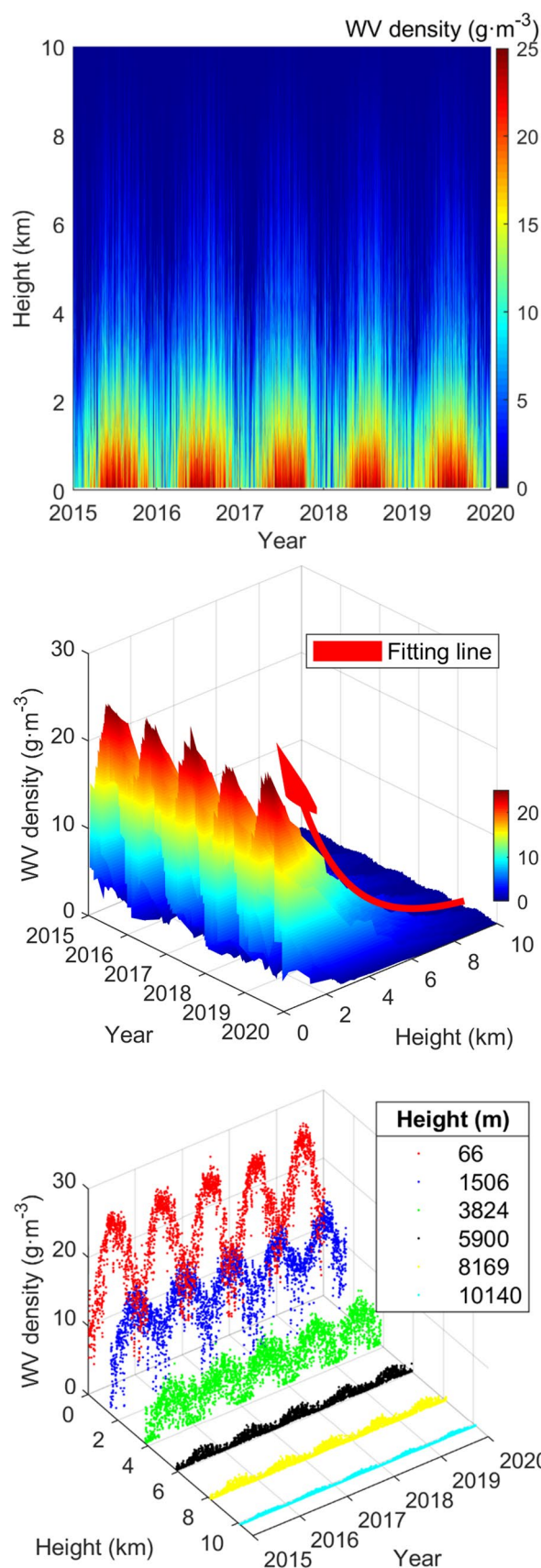


Fig. 4 Period analysis of surface WV density and PWV during 2015–2019. Left panels present the time series of the surface WV density and PWV and right panels their corresponding power spectrums, respectively. Additionally, the horizontal dashed lines in the right panels express 99% of the peak values

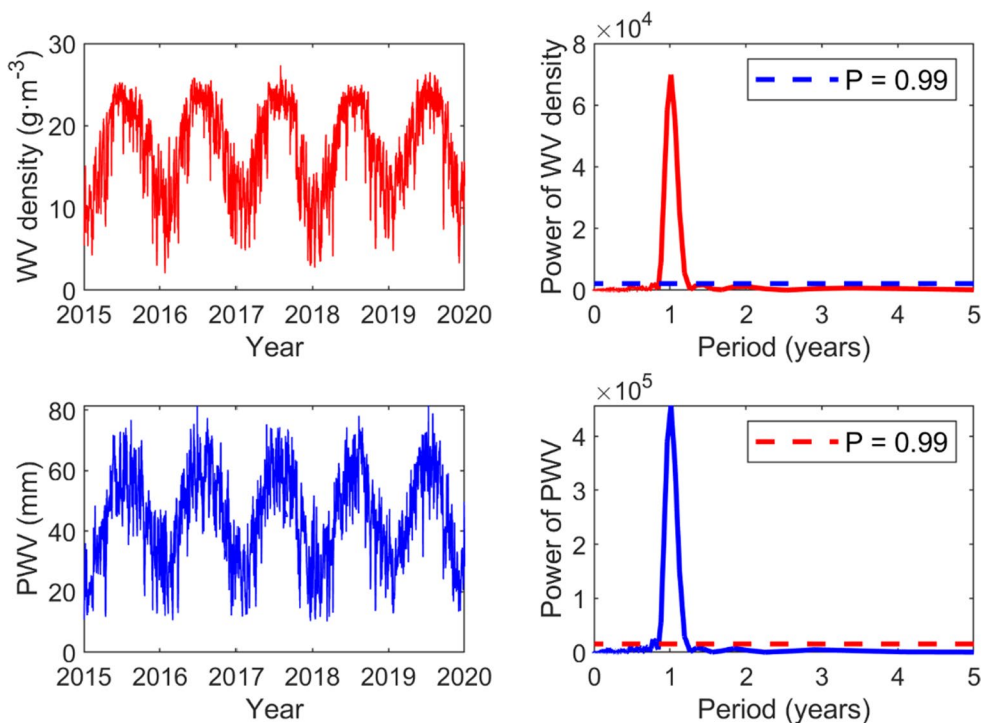
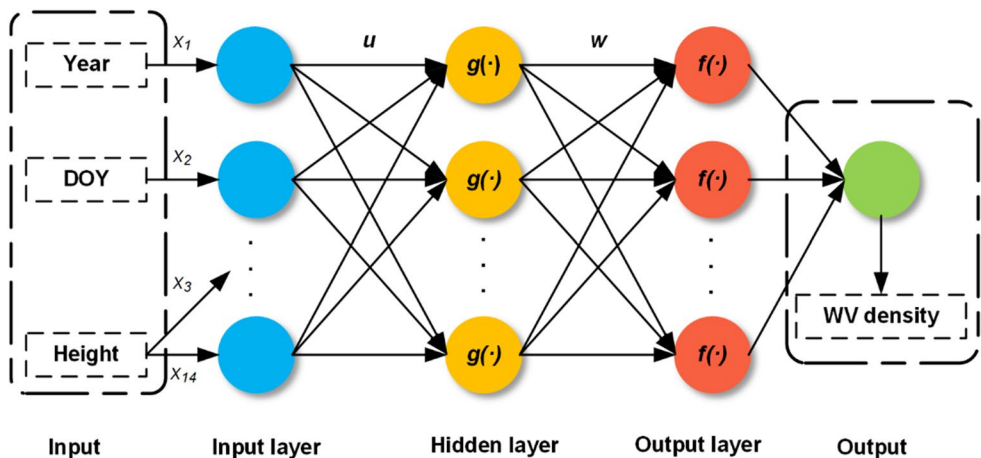


Fig. 5 Structure of the BPNN designed for WV density estimation. The symbols u and w represent the weights between the input and hidden layers and between the hidden and output layers, respectively. Additionally, $g(\cdot)$ and $f(\cdot)$ are the activation function of each neuron in the hidden layer and output layer, respectively



Bias comparison

Figure 7 displays the bias distributions of the CO and NN models. The bias of both models shows a similar distribution that decreases with increasing height. The spatial distribution of WV density was the primary reason for this phenomenon. The surface WV density, if affected by extreme weather, could be much larger or smaller than usual (model estimates), thus causing a significant bias. Conversely, at high altitudes, even a significant variation rate of WV density could cause a minor bias due to the limited content. In addition, combined with bias distribution (Fig. 8), the NN model has a lower bias with respect to the CO model in

general, suggesting that the NN model has a better predictive effect.

For a more detailed assessment of the model performance, the mean bias variations for both models with time and height are presented in Fig. 9. The top panel shows that the NN model obtains a lower bias (close to 0) than the CO model at most test epochs, indicating that the NN model obtains superior WV density estimates than the CO model. Moreover, we observe that the CO model shows more positive than negative bias. The bottom panel shows an apparent difference between the mean bias of the two models in views of height. For the CO model, a positive bias occurred below approximately 3.5 km, while a negative bias emerged at the

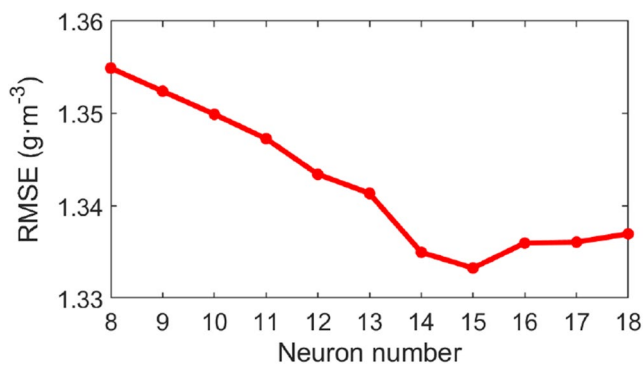


Fig. 6 Comparisons of RMSE from tenfold cross-validation using BPNNs with different numbers of hidden nodes

remaining height layers, revealing that the CO model underestimates the WV density at the surface but overestimates that for the rest of the troposphere. Meanwhile, the positive absolute value (near the surface) is greater than the negative (middle to top troposphere). It explains why the CO model appeared more positive bias (top panel). Contrary to the CO model, the bias of the NN model is negative below 3.5 km and positive at the other height layers, while the absolute values of the positive and negative biases are approximately equal. This result indicates that the NN model, in general, provides unbiased estimates of WV density.

Overall, combined with Figs. 7, 8, 9, the NN model achieves a superior prediction performance than the CO model in terms of bias. The reason for the low performance of the CO model may be that the traditional exponential model cannot reasonably describe the spatial distribution of the WV density, especially near the surface.

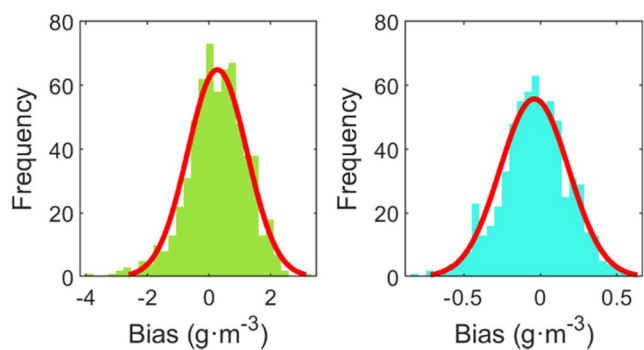
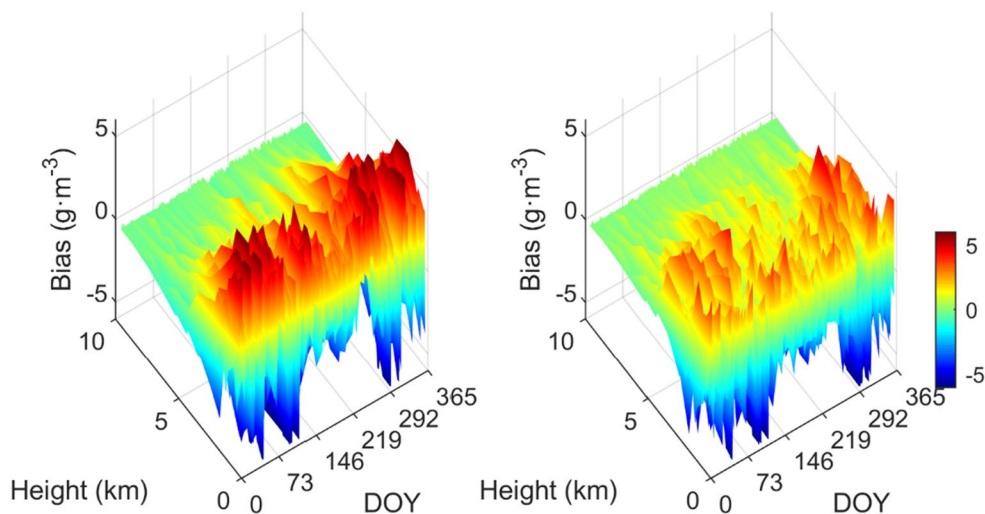


Fig. 8 Histogram of bias distribution for the CO model (left) and NN model (right)

RMSE comparison

In Fig. 10 (top), we observed that the RMSE for both models present similar temporal trends. Meanwhile, the NN model exhibits a smaller RMSE in most experimental periods compared with the CO model. It leads to that the NN model (red dashed line) has a lower mean RMSE than the CO model (blue dashed line). Besides, the maximum values for the blue and red lines were found at DOY 104 and 297 in 2020, respectively. As a result, the worst performance occurred on April 13, 2020, for the CO model, and October 23, 2020, for the NN model, respectively. According to the meteorological records, the above dates were the periods when HK suffered from extreme weather. It suggests that the poor performance of both models is caused by extreme weather. Besides, the bottom panel shows that the NN model performs better than the CO model at any height.

Fig. 7 Spatio-temporal distribution of bias for the CO model (left) and NN model (right). Notably, the bias here represents the deviation between the truth value originating from the RS observations and the estimated value from the WV density model



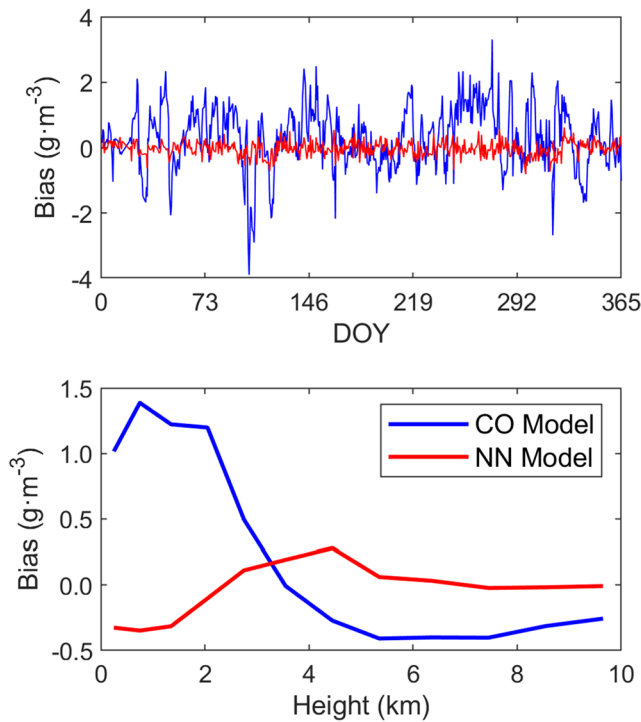


Fig. 9 Mean bias comparison of the CO model and the NN model at each DOY (top) and each height (bottom)

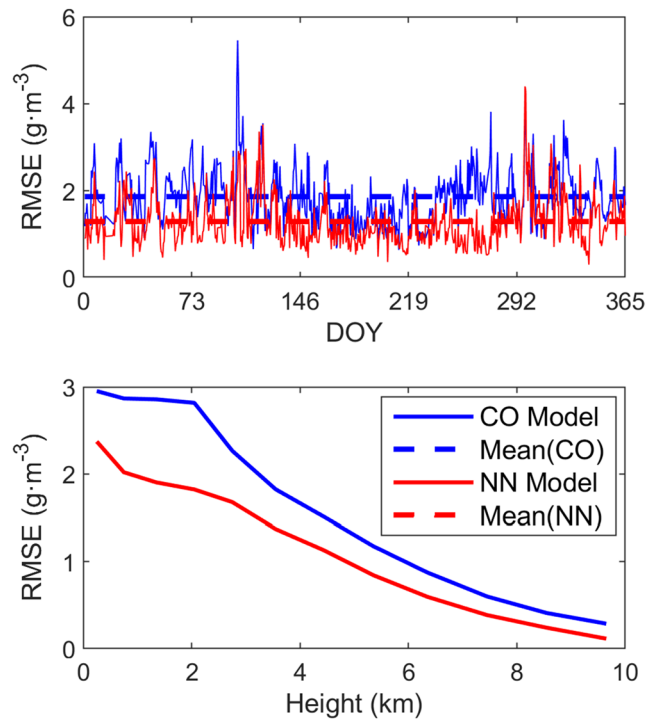


Fig. 10 RMSE comparison between the CO and NN models in terms of DOY (top) and height (bottom)

Overall performance

Table 1 shows that the overall bias and RMSE for the CO model are 0.3 and 1.9 g/m³, respectively, while they were reduced to 0.0 and 1.3 g/m³ for the NN model. This result indicates that the NN model exhibits a 100 and 32% improvement compared with the CO model in bias and RMSE. Based on the analysis above, we can conclude that the NN model has significantly better performance in the HK region than the CO model.

WV tomography experiments

To test the ability of the proposed model-based GNSS tomography in calibrating the poor initial values, we designed and conducted tomography experiments under severe weather conditions.

Text period selection and data preprocessing

As shown in Fig. 10 and Table 1, both the CO and NN models achieved a good prediction accuracy (low RMSE) at most test epochs. In particular, the RMSE of the NN model is less than 1.3 g/m³ for some experimental periods, suggesting that the initial values provided by the models alone are better

than the partially reported tomographic results (Dong and Jin 2018; Yao et al. 2020b; Zhao et al. 2020). However, the predictions of both two models deteriorated sharply during extreme weather, with the worst occurring at DOY 104 for the CO model and DOY 297 for the NN model.

The above periods are theoretically the best choice for testing the effects of the GNSS tomography. Therefore, we collected the GNSS observations and RS records in DOY 103–105 and 296–298, 2020. The former was processed by GAMIT/GLOBK (v 10.71) (Herring et al. 2018) to retrieve the SWV of each GNSS-ray path. Meanwhile, the latter is regarded as the actual values to verify the resultant GNSS-derived WV density.

Voxel strategy

As shown in Fig. 11 (left), we adopt the voxel division scheme in which seven and eight grids are in the latitudinal and longitudinal directions, respectively. Meanwhile, 12 layers are in the elevation direction, with thicknesses of 0.5, 0.5,

Table 1 Statistical results of the overall accuracy of the two models during the experimental period (g/m³)

	Bias	RMSE
CO model	0.3	1.9
NN model	0.0	1.3

0.7, 0.7, 0.7, 0.9, 0.9, 0.9, 1.1, 1.1, 1.1, and 1.1 km. After gridding, the selected tomographic area was discretized into $7 \times 8 \times 12$ voxels (right panel). Based on the divided voxels, we assembled and then solved the tomography equation (see section on GNSS troposphere WV tomography).

Tomographic results

The RMSE and absolute bias were selected to illustrate the calibration of the GNSS tomography technique on the initial WV density provided by the proposed models.

Calibration in RMSE

Figure 12 shows the RMSE of the proposed models and the calibrated results processed by GNSS tomography. For brevity, we simplified the CO model-based and the NN model-based GNSS tomography to the GNSS_CO method and GNSS_NN method, respectively. We found that when the NN model provides a better initial WV field, the GNSS_NN approach also exhibits better performance (lower RMSE) for most test epochs. The same can be stated for the CO model. This finding indicates that a better initial value drives better correction results regarding the GNSS tomography algorithm and vice versa.

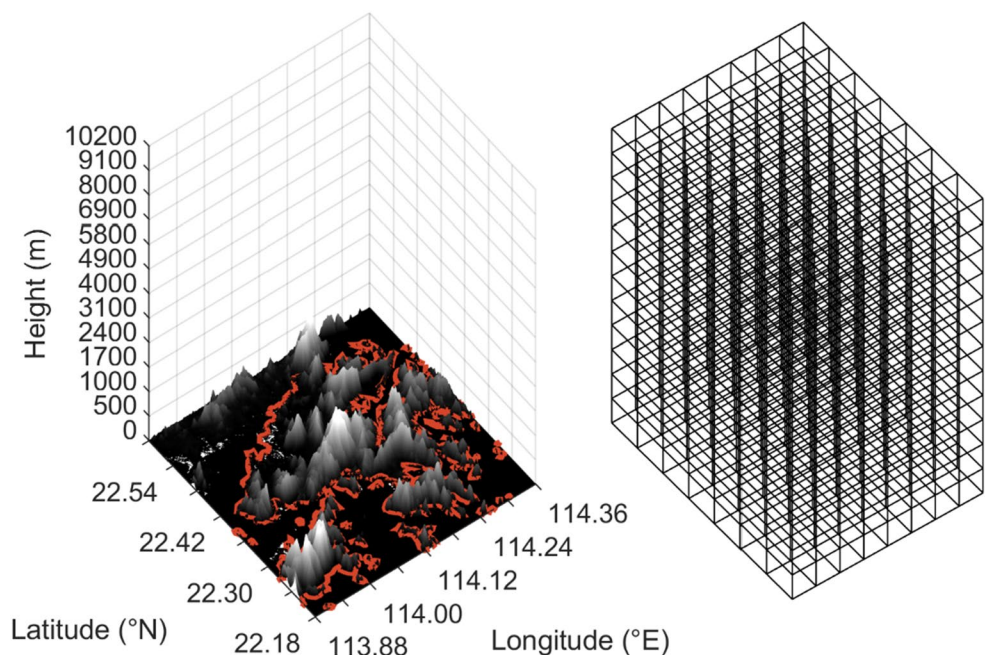
The RMSE reduces after the adjustment by the GNSS tomography. However, it was not significant in some cases (last six epochs). Figure 13 may explain this phenomenon, i.e., the GNSS tomography technique fails to accurately sense irregular distribution of WV caused by extreme weather. According to the weather record, under the

influence of a continental airstream behind the cold front, the weather in HK became very dry on DOY 102–103, 2020. Accordingly, the WV content shows an abnormally low value (black line in top panel). In these cases, both models overestimate the WV content, especially the CO model. Because of the low content WV, a minor adjustment will significantly reduce RMSE. Thus, we can observe that GNSS tomography receives a good optimization effect against the bad prior value (red and blue dash) in the first four cases. Unfortunately, the optimized WV profile (red and blue line) does not well match the actual value (black line).

The situation is quite different for the last six epochs. Figure 13 (bottom) displays the WV profiles (red and blue dash) that are calibrated by the GNSS tomography to the correct direction (near the black line). Unfortunately, due to the rich content and unusual distribution of WV below 3 km, i.e., low content at the surface and high in the middle troposphere, even with some correction, the adjusted profiles (red and blue lines) still differ significantly from their actual distribution (black line). Hence, the RMSE of both the GNSS_CO and GNSS_NN methods does not decrease significantly. Overall, the insensitivity to the abnormal distribution of WV caused the poor performance of the GNSS tomography.

Figure 14 illustrates the height variations of the RMSE for the GNSS_CO and GNSS_NN approaches. The RMSEs of both GNSS_CO and GNSS_NN exhibit a similar trend; with the increasing height, the RMSE decreases first and increases until reaching a peak, then overall decrease to the end. Furthermore, two peaks occur at the surface and the middle-low troposphere (approximately 2–4 km),

Fig. 11 Voxel strategy of the study area. The HK domain is divided into a 7×8 grid, and each grid spans 0.06° in latitude and longitude. Furthermore, 12 layers are designed for the vertical direction with the thicknesses of 0.5, 0.5, 0.7, 0.7, 0.7, 0.9, 0.9, 0.9, 1.1, 1.1, 1.1, and 1.1 km. After gridding (left), the study area is discretized to $7 \times 8 \times 12$ voxels (right)



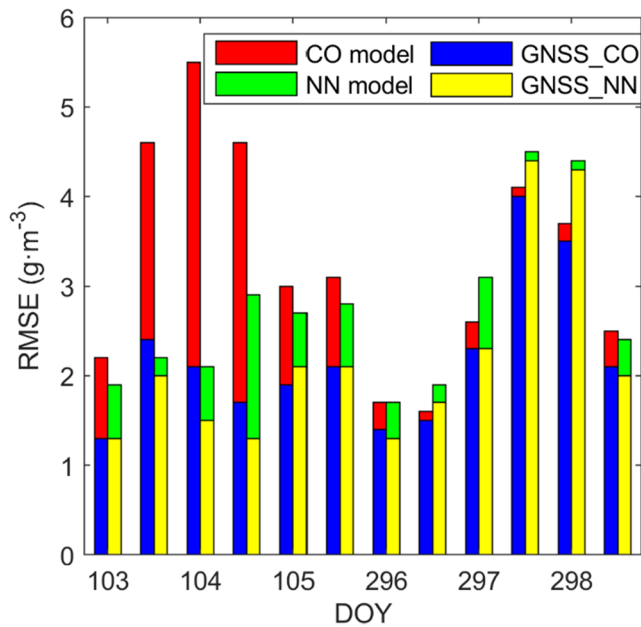


Fig. 12 RMSE comparison of the WV fields before and after GNSS tomography correction during DOY 103–105 and 296–298, 2020. Two proposed models generate the prior WV fields, respectively, and both are then adjusted by GNSS tomography. Here we define the tomography experiment for which the CO model provides initial values as the GNSS_CO method. Accordingly, the GNSS_NN method refers to the GNSS tomography based on the NN model

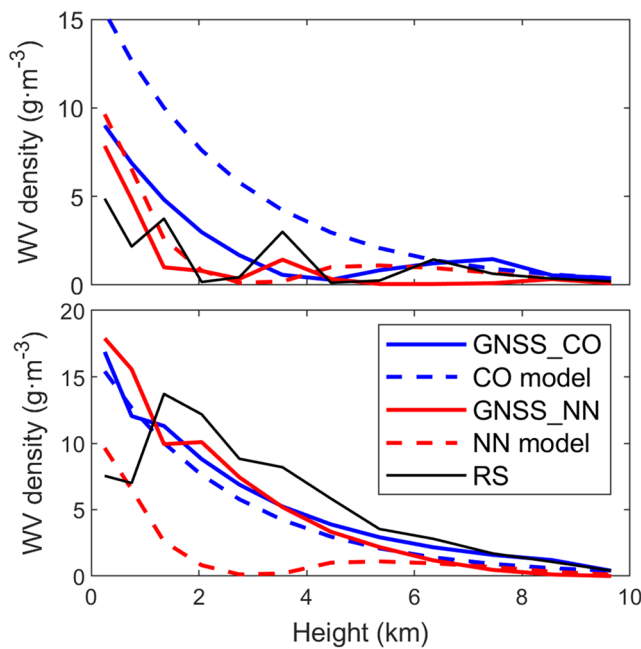


Fig. 13 Comparison of WV profiles obtained by RS, CO model, NN model, GNSS_CO method, and GNSS_NN method at UTC 00:00 of DOY 104, 2020 (top), and DOY 298, 2020 (bottom)

respectively. The results suggest that the two above methods have the worst performance at the surface, followed by the middle-low troposphere. Recalling Fig. 13, we realize that the WV content at the surface is lower than expected, while the middle is abnormally high. It demonstrates again that GNSS tomography has not effectively captured the anomalous distribution of WV, which is the key reason for its poor predicted performance.

Calibration in absolute bias

For a comprehensive evaluation of the applicability of GNSS tomography under extreme weather conditions, the absolute bias comparison between the original WV fields and their calibrated results is shown in Fig. 15. It is noticed that after the GNSS tomography adjustment, the absolute bias of the WV fields significantly reduces in all test epochs, and the maximum improvement is up to 95%. This result suggests that the GNSS tomography technique can accurately correct the overall WV content. Combining Figs. 12, 13, 14, 15, we can conclude that the GNSS tomography technique can correct the variation of WV content caused by extreme weather, but not its irregular distribution.

Conclusions and outlooks

We proposed the CO and NN models for the initial WV density estimation used in GNSS troposphere tomography. The CO model consists of an exponential and a linear least-squares model, while the NN model is BPNN-based. WV density originating from HK RS during 2015–2019 is the common modeling data for both models.

First, we adopted RS-derived WV density datasets for 2020 to validate the two proposed models. Statistical results indicated that compared with the CO model, the NN model exhibited 32% accuracy improvements in terms of RMSE.

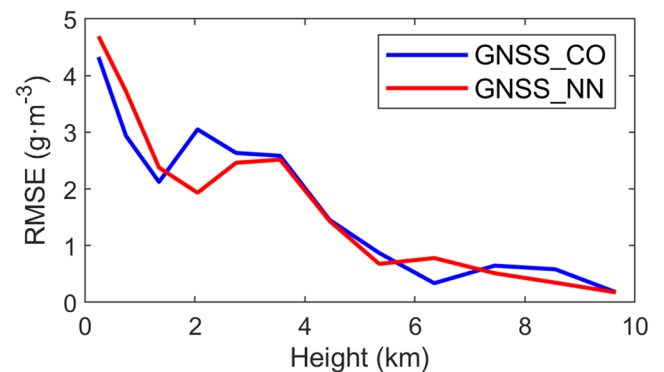


Fig. 14 Variation in RMSE with height for the GNSS_CO and GNSS_NN approaches during the test period

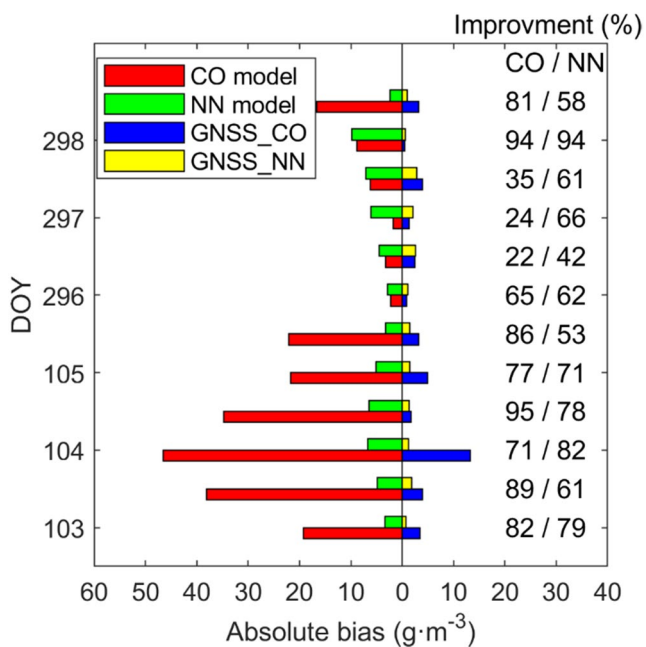


Fig. 15 Absolute bias comparison between prior WV fields and their calibrated results processed by GNSS tomography for the test period. Furthermore, the accuracy improvements of the WV density after tomography correction are listed on the right side of the figure

In addition, the bias distribution revealed that the CO model underestimated the WV density. However, the NN model provided unbiased estimates of the WV density.

Second, two periods were selected to investigate the applicability of the proposed model-based GNSS tomography in extreme weather conditions. The one is April 12–14, 2020, and the other is October 22–24, 2020. Test results suggested that the tomography technique could significantly modify the incorrect WV content but not accurately adjust the WV distribution. Therefore, accurately sensing the irregular distribution of the WV remains a challenge for GNSS WV tomography.

Currently, both the CO and NN models only support the regional WV density estimation. Hence, future work will focus on establishing an updated version for global users. For the tomography algorithm, further improvement will highlight a reasonable spatial voxel scheme and vertical constraint, increasing its detection ability for 3D WV information during extreme weather.

Acknowledgements We would like to thank the International GNSS Service (IGS), Survey and Mapping Office of the Lands Department (SMOLD) of HK, and HK Observatory (HKO) for the provision of data and products. This research was funded by the National Natural Science Foundation of China (41721003), and the Guangxi Key Laboratory of Spatial Information and Geomatics (19-185-10-17). This work was also supported by the Key Technology Projects of Transportation Industry (2019-MS1-013), and the Science and Technology Project of

Highway Construction Engineering of Zhejiang Provincial Department of Transportation (2019-GCKY-02). Our deepest gratitude goes to the anonymous reviewers for their careful work and thoughtful suggestions that have helped improve this paper substantially.

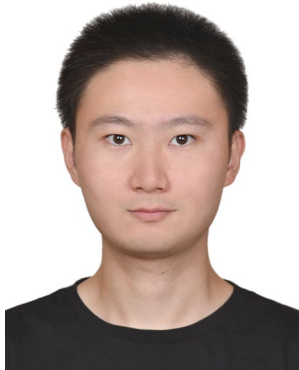
Data availability HK radiosonde (station code: 45004) records are available at <http://weather.uwyo.edu/upperair/sounding.html>. The GNSS observations of SatRef can be downloaded at <http://www.geodetic.gov.hk/en/rinex/downv.aspx>. The GAMIT/GLOBK software used in this study can be freely accessed at <http://geoweb.mit.edu/gg>.

References

- Bender M et al (2011) Development of a GNSS water vapour tomography system using algebraic reconstruction techniques. *Adv Space Res* 47:1704–1720
- Bevis M, Businger S, Herring TA, Rocken C, Anthes RA, Ware RH (1992) GPS meteorology: remote sensing of atmospheric water vapor using the Global Positioning System. *J Geophys Res Atmos* 97:15787–15801
- Chen B, Liu Z (2014) Voxel-optimized regional water vapor tomography and comparison with radiosonde and numerical weather model. *J Geod* 88:691–703
- Chen B, Liu Z (2016) Assessing the performance of troposphere tomographic modeling using multi-source water vapor data during Hong Kong's rainy season from May to October 2013. *Atmos Meas Tech* 9:5249–5263
- Dai A, Wang J, Ware RH, Van Hove T (2002) Diurnal variation in water vapor over North America and its implications for sampling errors in radiosonde humidity. *J Geophys Res Atmos* 107:ACL 11–11–ACL 11–14
- Ding M (2018) A neural network model for predicting weighted mean temperature. *J Geod* 92:1187–1198
- Ding W, Wang J, Rizos C, Kinlyside D (2007) Improving adaptive Kalman estimation in GPS/INS integration. *J Navig* 60:517–529
- Dong Z, Jin S (2018) 3-D water vapor tomography in Wuhan from GPS BDS and GLONASS observations. *Remote Sens* 10:62
- Elosegui P, Ruis A, Davis J, Ruffini G, Keihm S, Bürki B, Kruse L (1998) An experiment for estimation of the spatial and temporal variations of water vapor using GPS data. *Phys Chem Earth* 23:125–130
- Flores A, Ruffini G, Rius A (2000) 4D tropospheric tomography using GPS slant wet delays. *Ann Geophys* 18:223–234
- Gradinarsky LP, Jarlemark P (2004) Ground-based GPS tomography of water vapor: analysis of simulated and real data. *J Meteorol Soc Jpn* 82:551–560
- Gurbuz G, Jin S (2017) Long-time variations of precipitable water vapour estimated from GPS, MODIS and radiosonde observations in Turkey. *Int J Climatol* 37:5170–5180
- Haykin S (1998) *Neural networks: a comprehensive foundation*, 2nd edn. Prentice Hall, Upper Saddle River
- Herring T, King R, Floyd M, McClusky S (2018) *GAMIT reference manual, GPS analysis at MIT*. Department of earth, atmospheric, and planetary sciences, Massachusetts Institute of Technology
- Hocke K (1998) Phase estimation with the Lomb-Scargle periodogram method. *Ann Geophys* 16:356–358
- Masters T (1994) *Practical neural network recipes in C++*. Academic Press, Boston
- Nilsson T, Gradinarsky L (2006) Water vapor tomography using GPS phase observations: simulation results. *IEEE Trans Geosci Remote Sens* 44:2927–2941
- Rocken C et al (1993) Sensing atmospheric water vapor with the Global Positioning System. *Geophys Res Lett* 20:2631–2634

- Tomasi C (1981) Determination of the total precipitable water by varying the intercept in Reitan's relationship. *J Appl Meteorol Climatol* 20:1058–1069
- Troller MR (2004) GPS based determination of the integrated and spatially distributed water vapor in the troposphere. *ETH Zurich*
- Yao Y, Liu C, Xu C (2020a) A new GNSS-Derived water vapor tomography method based on optimized voxel for large GNSS network. *Remote Sens* 12:2306
- Yao Y, Liu C, Xu C, Tan Y, Fang M (2020b) A refined tomographic window for GNSS-Derived water vapor tomography. *Remote Sens* 12:2999
- Zhang B, Yao Y (2021) Precipitable water vapor fusion based on a generalized regression neural network. *J Geod* 95:1–14
- Zhang L, Wang F, Sun T, Xu B (2018) A constrained optimization method based on BP neural network. *Neural Comput Appl* 29:413–421
- Zhao Q, Yao Y, Yao WQ, Li Z (2018) Near-global GPS-derived PWV and its analysis in the El Niño event of 2014–2016. *J Atmos Sol Terr Phys* 179:69–80
- Zhao Q, Yao W, Yao Y, Li X (2020) An improved GNSS tropospheric tomography method with the GPT2w model. *GPS Solut* 24:1–13
- Zhao Q, Liu Y, Yao W, Yao Y (2021) Hourly rainfall forecast model using supervised learning algorithm. *IEEE Trans Geosci Remote Sens*. <https://doi.org/10.1109/TGRS.2021.3054582> (in press)

Publisher's Note Springer Nature remains neutral with regard to jurisdictional claims in published maps and institutional affiliations.



Chen Liu is currently working toward a Ph.D. degree in Geodesy and Surveying Engineering from the Wuhan University, China. He received an M.Sc. degree from the China University of Mining and Technology, China, in 2019. His research interests include GNSS data processing and 3D tropospheric tomography.



Yibin Yao obtained his Ph.D. degree in Geodesy and Surveying Engineering from the Wuhan University, China, in 2004 and is a Professor at the School of Geodesy and Geomatics, Wuhan University, China. His current research interests include GNSS ionospheric, tropospheric and meteorological studies, and high-precision GNSS data processing.



Chaoqian Xu received a Ph.D. degree in Geodesy and Surveying Engineering from the Wuhan University, China, in 2017 and is a postdoctoral scholar at the School of Geodesy and Geomatics, Wuhan University, China. His main research interest includes real-time high-precision GNSS positioning and method of surveying data processing.